

## Article

# Piezoelectric and Pyroelectric Properties of Organic MDABCO-NH<sub>4</sub>Cl<sub>3</sub> Perovskite for Flexible Energy Harvesting

Rosa M. F. Baptista <sup>1,\*</sup>, Bruna Silva <sup>1</sup>, João Oliveira <sup>1</sup>, Bernardo Almeida <sup>1</sup>, Cidália Castro <sup>2</sup>, Pedro V. Rodrigues <sup>2</sup>, Ana Machado <sup>2</sup>, Etelvina de Matos Gomes <sup>1</sup> and Michael Belsley <sup>1,\*</sup>

<sup>1</sup> Centre of Physics of Minho and Porto Universities (CF-UM-UP), Laboratory for Materials and Emergent Technologies (LAPMET), Campus de Gualtar, University of Minho, 4710-057 Braga, Portugal; brunasilva@fisica.uminho.pt (B.S.); b8171@fisica.uminho.pt (J.O.); bernardo@fisica.uminho.pt (B.A.); emg@fisica.uminho.pt (E.d.M.G.)

<sup>2</sup> Institute for Polymers and Composites, Campus de Azurém, University of Minho, 4800-058 Guimarães, Portugal; cidaliacastro@dep.uminho.pt (C.C.); pedro.rodrigues@dep.uminho.pt (P.V.R.); avm@dep.uminho.pt (A.M.)

\* Correspondence: rosa\_baptista@fisica.uminho.pt (R.M.F.B.); belsley@fisica.uminho.pt (M.B.)

**Abstract:** This study describes the synthesis and characterization of the lead-free organic ferroelectric perovskite *N*-methyl-*N'*-diazabicyclo [2.2.2]octonium)-ammonium trichloride (MDABCO-NH<sub>4</sub>Cl<sub>3</sub>). The electrospinning technique was employed to obtain nanofibers embedded with this perovskite in a PVC polymer for hybrid fiber production. The dielectric, piezoelectric, and pyroelectric properties of these fibers were carefully examined. Based on measurements of the dielectric permittivity temperature and frequency dependence, together with the pyroelectric results, a transition from a high temperature paraelectric to a ferroelectric phase that persisted at room temperature was found to occur at 438 K. The measured pyroelectric coefficient yielded values as high as 290 μC K<sup>-1</sup> m<sup>-2</sup>, which is in between the values reported for MDABCO-NH<sub>4</sub>I<sub>3</sub> and the semiorganic ferroelectric triglycine sulfate (TGS). The hybrid nanofibers exhibited good morphological characteristics and demonstrated very good piezoelectric properties. Specifically, a piezoelectric coefficient of 42 pC/N was obtained when applying a periodical force of 3 N and a piezoelectric voltage coefficient of  $g_{\text{eff}} = 0.65 \text{ V mN}^{-1}$ . The performance of these fibers is on par with that of materials discussed in the existing literature for the fabrication of nano energy-harvesting generators. Importantly, the perovskite nanocrystals within the fibers are protected from degradation by the surrounding polymer, making them a promising environmentally friendly platform for flexible mechanical energy harvesting.

**Keywords:** organic perovskite; electrospinning; fibers; piezoelectricity; pyroelectricity; nano energy harvesting



**Citation:** Baptista, R.M.F.; Silva, B.; Oliveira, J.; Almeida, B.; Castro, C.; Rodrigues, P.V.; Machado, A.; Gomes, E.d.M.; Belsley, M. Piezoelectric and Pyroelectric Properties of Organic MDABCO-NH<sub>4</sub>Cl<sub>3</sub> Perovskite for Flexible Energy Harvesting. *Micro* **2024**, *4*, 196–205. <https://doi.org/10.3390/micro4020014>

Academic Editor: Hiroshi Furuta

Received: 7 February 2024

Revised: 14 March 2024

Accepted: 25 March 2024

Published: 27 March 2024



**Copyright:** © 2024 by the authors. Licensee MDPI, Basel, Switzerland. This article is an open access article distributed under the terms and conditions of the Creative Commons Attribution (CC BY) license (<https://creativecommons.org/licenses/by/4.0/>).

## 1. Introduction

Ferroelectric materials, characterized by their simultaneous pyroelectric and piezoelectric properties stemming from spontaneous polarization that can be switched by applying an external static electric field, represent a crucial area of research in materials science. Within this domain, inorganic perovskites of the ABX<sub>3</sub> type (where A and B are metal cations, and X is typically an oxide anion) have been studied extensively, with notable examples including strontium titanate (SrTiO<sub>3</sub>), barium titanate (BaTiO<sub>3</sub>), lithium niobate (LiNbO<sub>3</sub>), and lead titanate (PbTiO<sub>3</sub>) [1]. The ability of these metal oxides to accommodate a variety of anionic or cationic substitutions facilitates the tuning of their piezoelectric and pyroelectric properties, with the potential to enhance their photo-electric conversion abilities and photocatalytic responses [2–4]. At the moment, the piezoelectrics available on the market are predominantly inorganic perovskites, particularly materials based on lead zirconate titanate (PZT). However, inorganic perovskites typically contain heavy metals, making them environmentally unfriendly, with lead-bearing compounds being particularly

toxic. In addition, they are generally processed at high temperatures and brittle, making them unsuitable for flexible mechanical-energy-harvesting applications.

One way of avoiding the toxicity of lead-based perovskites is the substitution of either the ions A or X in perovskite-type materials with a molecular building unit [5,6], a possibility that is actively being investigated by several research groups. These hybrid perovskites offer several advantages over their inorganic counterparts, including ease of synthesis at room temperature, greater flexibility, and reduced weight. Their unique structural variability enables highly tunable properties, making them attractive candidates for various applications, particularly in the realm of pyroelectric and piezoelectric technologies, where they have the potential to replace inorganic materials [7–10]. Since the discovery of the first semi-organic ferroelectric, Rochelle salt (or sodium potassium tartrate tetrahydrate [KNaC<sub>4</sub>H<sub>4</sub>O<sub>6</sub> (4H<sub>2</sub>O)]), by Valasek in 1920, these materials have been a focal point of fundamental and applied research [11,12].

Optoelectronic devices employing semi-organic crystalline materials are often competitive with respect to their inorganic counterparts. They have become a focal point of research in developing new piezoelectric and pyroelectric materials able to replace their traditional inorganic counterparts [7–10]. Crucially, the pursuit of lead-free alternatives gained momentum from the discovery of remarkably efficient solar cells incorporating methylammonium lead halide perovskites. This breakthrough prompted the exploration of lead-free hybrid organic–inorganic perovskites, a new promising branch within the perovskite domain [13–18].

The exploration of nanoscale ferroelectrics, particularly in the form of electrospun nanofibers [19–23], holds significant potential for enhancing mechanical strength and flexibility while leveraging their pyroelectric and piezoelectric properties. In this regard, the exploration of nanoscale ferroelectrics with a perovskite structure is a promising and vital endeavor, as indicated by previous studies [7,24]. One promising application of functional electrospun fibers is the collection of electrical nano energy at low frequencies through the piezoelectric effect [25].

One promising example of a lead-free organic-inorganic perovskite is MDABCO-NH<sub>4</sub>I<sub>3</sub> (N-methyl-N'-diazabicyclo[2.2.2]octonium)-ammonium triiodide [26]. This material displays an impressive spontaneous polarization of 22  $\mu\text{C}/\text{cm}^2$ , comparable to that of traditional inorganic ferroelectrics like BaTiO<sub>3</sub> at 26  $\mu\text{C}/\text{cm}^2$ . With a ferroelectric–paraelectric phase transition taking place at 448 K and displaying multiple polarization directions, MDABCO-NH<sub>4</sub>I<sub>3</sub> exhibits attractive characteristics for integration in cutting-edge flexible optoelectronic devices [27,28]. Nanocrystals of this compound were successfully embedded into electrospun polymer fibers and demonstrated the ability to serve as promising flexible energy-harvesting sources, exhibiting a piezoelectric voltage coefficient of  $g_{\text{eff}} = 3.6 \text{ V mN}^{-1}$  and a pyroelectric coefficient as high as 194  $\mu\text{C K}^{-1} \text{ m}^{-2}$ .

By substituting the iodine atoms in MDABCO-NH<sub>4</sub>I<sub>3</sub> with bromine, a family-related compound, MDABCO-NH<sub>4</sub>Br<sub>3</sub>, can be obtained, which is isostructural with MDABCO-NH<sub>4</sub>I<sub>3</sub>, both crystallizing in the same space group, *R*3, at their room temperature ferroelectric phase and *P*432 high-temperature paraelectric phase [27]. Motivated by the similarities between these two compounds, we anticipated that if the iodine atoms in MDABCO-NH<sub>4</sub>I<sub>3</sub> were substituted with chlorine atoms, another family-related compound, MDABCO-NH<sub>4</sub>Cl<sub>3</sub>, would be obtained, and it would also have the potential to display outstanding pyroelectric and piezoelectric properties.

In this manuscript, we describe the successful production and characterization of the related perovskite, MDABCO-NH<sub>4</sub>Cl<sub>3</sub>, in electrospun poly(vinyl chloride) (PVC) polymer nanofibers. In particular, we demonstrate their potential as piezoelectric voltage converters or piezoelectric nanogenerators (PENGs) capable of efficient mechanical energy harvesting. Specifically, these flexible and lightweight electrospun fiber mats yield a piezoelectric coefficient of 42 pC/N under the influence of small (under 10 N) periodic mechanical forces. Significantly, the pyroelectric coefficient of electrospun fibers containing

polycrystalline MDABCO-NH<sub>4</sub>Cl<sub>3</sub> is comparable to that of the hybrid organic ferroelectric MDABCO-NH<sub>4</sub>I<sub>3</sub>.

## 2. Materials and Methods

### 2.1. Precursor Materials and Nanofibers Production

We produced the precursor (MDABCO)I by following the method outlined by Kreuer et al. [29]. Subsequently, MDABCO-NH<sub>4</sub>Cl<sub>3</sub> crystals were obtained following the method reported by You and Xiong [27]. To achieve particle sizes smaller than 40 μm, the MDABCO-NH<sub>4</sub>Cl<sub>3</sub> crystals were ground and sieved.

All chemicals and solvents, obtained from Sigma-Aldrich (Schenldorf, Germany), were used without any further purification. High-molecular-weight polyvinyl chloride (PVC), with a density of 1.40 g/mL, was supplied by Janssen (Beerse, Belgium). To prepare the 10% PVC electrospinning precursor solution, the pellets were dissolved in a solvent mixing system consisting of 5 mL of tetrahydrofuran (THF) and dimethylformamide (DMF) in a 50:50 (*v/v*) ratio. After complete dissolution, MDABCO-NH<sub>4</sub>Cl<sub>3</sub>, in a ratio of 1:5 by weight, was added in small portions, and the resulting solution was stirred for several hours under ambient conditions before the electrospinning process. The initial step involved loading a 5 mL syringe with the precursor solution. Attached to the syringe was a needle with inner and outer diameters of 0.232 mm and 0.5 mm, respectively. The anode of a high-voltage power supply (Spellmann CZE2000) provided a positive bias to the syringe needle.

Preferentially aligned fiber mats composed of PVC polymer with and without embedded MDABCO-NH<sub>4</sub>Cl<sub>3</sub> perovskite were fabricated using an E-Fiber EF100 (Leonardino Srl/SKE Research Equipment<sup>®</sup>, Milan, Italy) electrospinning apparatus in a horizontal configuration. Several key elements comprise the production process. A high-voltage power supply provided a 20 kV bias between the syringe metal tip and a grounded rotating drum collector, which were 13 cm apart. The polymer solution flow rate was consistently maintained at 0.18–0.20 mL/h as it was extruded through the spinneret using a precise syringe pump. A variable motor-speed controller regulated the rotation of the drum collector. Aluminum foil covering the collector amassed the fibers produced.

### 2.2. Scanning Electron Microscopy (SEM)

A Nova Nano SEM 200 scanning electron microscope (FEI Company, Hillsboro, OR, USA) was employed to examine the MDABCO-NH<sub>4</sub>Cl<sub>3</sub> perovskite nanofibers' morphology, size, and shape. Operating at an acceleration voltage of 10 kV, the instrument facilitated detailed analysis. To prepare the nanofibers for analysis, they were deposited onto a silica surface, pre-coated with a 10 nm thick Au-Pd (80–20 weight %) film. A high-resolution sputter coater, specifically the 208HR from Cressington Company (Watford, UK), coupled with a Cressington MTM-20 high-resolution thickness controller facilitated a controlled gold film deposition.

The nanofiber's diameters were determined based on the scanning electron microscope images using the open-source image-processing software ImageJ 1.51n (ImageJ2, NIH, <https://imagej.nih.gov/ij/>, accessed on 12 January 2024). To establish the average fiber diameter and the fiber diameter distribution, 50 nanofibers were randomly selected in the SEM images. We fitted the distribution of the measured fiber diameters to a log-normal function.

### 2.3. X-ray Diffraction and Raman Spectroscopic Measurements

The investigation into the crystallinity and crystallographic orientation of MDABCO-NH<sub>4</sub>Cl<sub>3</sub> within the fibers involved X-ray diffraction. Here,  $\theta$ – $2\theta$  scans were conducted. A Bruker D8 Discover X-ray diffractometer (Bruker, Madison, WI, USA) equipped with Cu-K $\alpha$  radiation (1.5406 Å wavelength) recorded the diffraction patterns.

#### 2.4. Dielectric Spectroscopy

The dielectric properties of MDABCO-NH<sub>4</sub>Cl<sub>3</sub> crystals were assessed through impedance spectroscopy between temperatures ranging from 300 to 450 K and over a 100 Hz–1 MHz frequency span. To determine the complex permittivity, denoted as  $\epsilon = \epsilon' - i\epsilon''$ , where  $\epsilon$  is the real component and  $\epsilon''$  is the imaginary component, the capacitance (C) and loss tangent ( $\tan \delta$ ) were measured. The following relations were used:

$$C = \epsilon\epsilon_0(\mathcal{A}/s) \quad \tan \delta = \epsilon''/\epsilon'$$

In these equations,  $\mathcal{A}$  signifies the area of electrical contact, while the fiber mat thickness is denoted by  $s$ . In the measurements, the sample was sandwiched between a cylindrical metal contact with an approximate diameter of  $10^{-2}$  m and the aluminum foil on which the fiber mats were collected. Altogether, this formed a parallel-plate capacitor integrated into the measurement LCR network. Measurements were conducted using a Wayne Kerr 6440A precision component analyzer (Wayne Kerr Electronics, Bognor Regis, UK), interfaced with a computer. A shielded test leads help mitigate parasitic impedances resulting from the electrical connections. Temperature-dependent measurements were executed at a rate of 2 °C/min, facilitated by a Polymer Labs PL706 PID controller (Polymer Labs, Los Angeles, CA, USA) and furnace.

#### 2.5. Pyroelectric Measurements

Pyroelectricity results from the temperature-dependent nature of spontaneous polarization, in which changes in temperature induce an electric field via changes in the intrinsic dipoles. The surface layer of free charges counteracts this electric field. The key parameter that characterizes this phenomenon is the pyroelectric coefficient, denoted by the rate of change in spontaneous polarization ( $p = dPs/dT$ ). Measuring the change in polarization involves monitoring the pyroelectric current ( $I = A(dPs/dT)(dT/dt)$ ) using a Keithley 617 electrometer (Keithley Instruments GmbH, Landsberg, Germany). Here, the electrode area is  $A$ , while the rate of temperature change is  $dT/dt$ . A capacitor geometry under short-circuit conditions was employed.

#### 2.6. Piezoelectric Measurements

To measure the piezoelectric output voltage and current of the fibers, we connected them to a 100 M $\Omega$  load resistance and transmitted the signals through a low-pass filter, subsequently amplifying them using a low-noise preamplifier (SR560, Stanford Research Systems, Stanford, CA, USA). All signals were recorded using a digital storage oscilloscope (Agilent Technologies DSO-X-3012A, Waldbronn, Germany). A vibration generator (SF2185, Frederiksen Scientific, Olgod, Denmark) subjected the fiber array sample, measuring (30 × 40) mm<sup>2</sup> with a thickness of 200  $\mu$ m, to periodic mechanical forces. The frequency of the applied forces, set at 3 Hz, was controlled by a signal generator (33120A, Hewlett Packard, Palo Alto, CA, USA). A force-sensing resistor (FSR402, Interlink Electronics Sensor Technology, Graefelfing, Germany) calibrated the applied forces. To ensure that the sample experienced consistent and perpendicular force application across its surface, the sample was carefully fixed on a stage mount.

### 3. Results and Discussion

#### 3.1. Dielectrics

The electric permittivity of MDABCO-NH<sub>4</sub>Cl<sub>3</sub> was measured as a function of temperature and frequency, that is, from room temperature to 453 K and at up to 3 MHz. Their real ( $\epsilon'$ ) and imaginary ( $\epsilon''$ ) components are shown in Figure 1a and 1b, respectively. The dielectric constant ( $\epsilon'$ ) decreases with an increasing frequency, with an initial shaper drop at low frequencies, transitioning to a slower variation at high frequencies. On the other hand, two maxima, marked with the letters A and B in Figure 1b, can be observed in the imaginary component of the electric permittivity, which are characteristic of the presence of

two dielectric relaxations. One occurs above 10 kHz (A relaxation), and the other occurs in the 10 Hz–1 kHz frequency region (B relaxation). These relaxations can be further observed in  $\epsilon'$ , as indicated by the appearance of two plateaus in the frequency intervals associated with the A and B maxima and by the appearance of two semi-circles in the Cole–Cole plots in Figure 1c. The rise in the dielectric constant values at the low-frequency end (Figure 1a) is influenced by the Maxwell–Wagner–Sillars polarization that occurs at the nanoscale, where the charge carriers can be blocked at the inner dielectric boundary layers or interfaces between grains in the polycrystalline MDABCO-NH<sub>4</sub>Cl<sub>3</sub> sample [30].

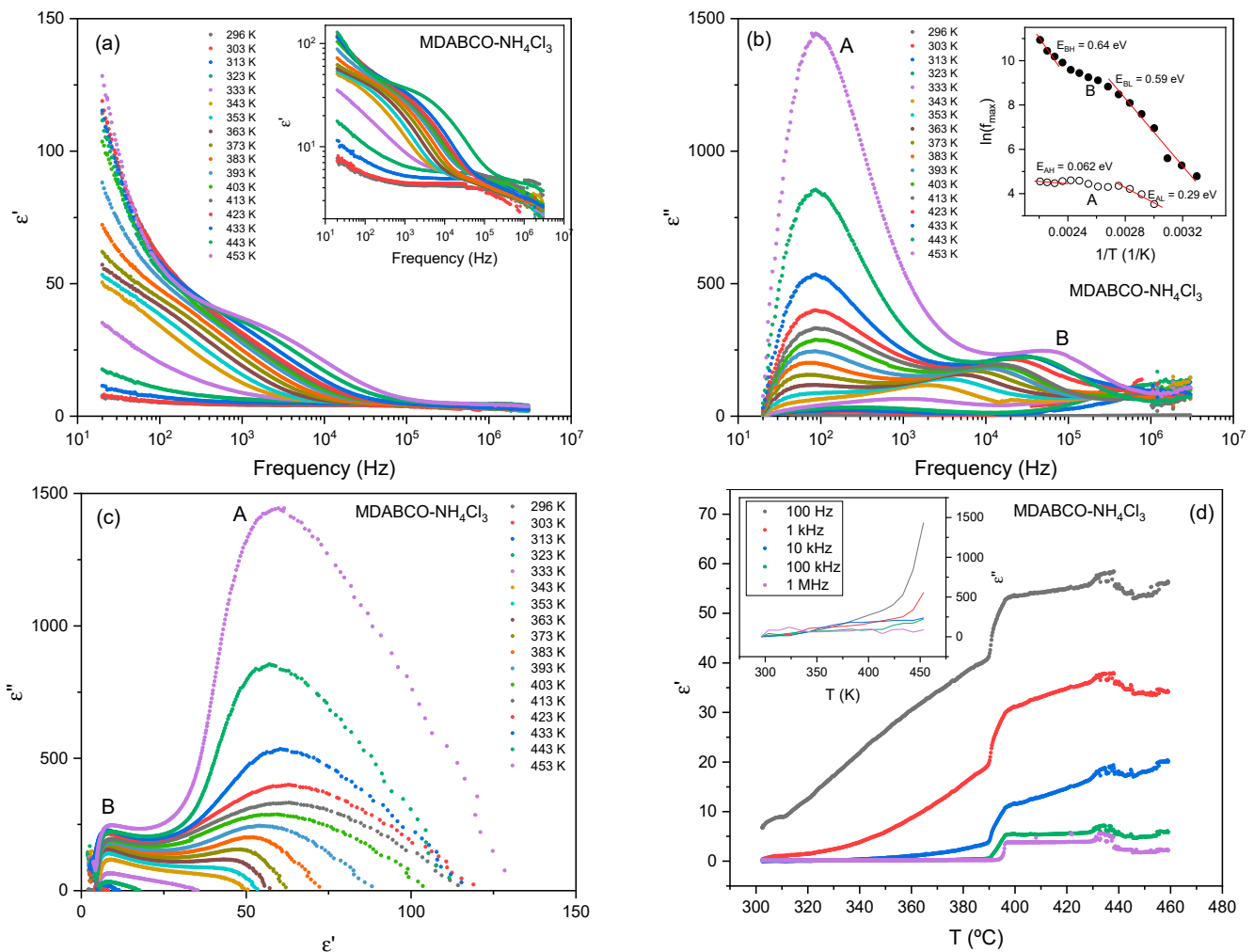


**Figure 1.** Frequency dependence of the (a) real part and (b) imaginary part of the dielectric permittivity polycrystalline MDABCO-NH<sub>4</sub>Cl<sub>3</sub>. (b) Inset plots of the logarithm of the frequency corresponding to the maximum of the relaxations marked with A (open dots) and B (closed dots) in  $\epsilon''$  versus the inverse of the temperature. The straight red lines are fits to the curves, which were used to obtain the corresponding activation energies. (c) The Cole–Cole plot and (d) temperature dependence of the real and imaginary (inset) components of the electric permittivity of the sample.

According to the following equation, the frequency of the maxima of the imaginary component of the dielectric permittivity ( $f_m$ ) is related to the relaxation time ( $\tau$ ) of the process:  $2\pi f_m \tau = 1$ . The frequency of the maxima follows a thermally activated Arrhenius-type behavior described by the following equation [30]:

$$f_m = f_{m0} \exp\left(-\frac{E}{k_B T}\right) \quad (1)$$

where  $f_m$  is the frequency of the maxima,  $f_{m0}$  is a constant,  $k_B$  is the Boltzmann constant, and  $E$  is the activation energy of the process. The result of taking the logarithm of Equation (1) is a linear dependence, which can be fit with a straight line according to the following expression:  $\ln(f_m) = \ln(f_{m0}) - \frac{E}{k_B T}$ . The inset of Figure 1b shows the linear fits to the graphics of  $\ln(f_m)$  as a function of the inverse of the temperature for both relaxations. For each curve, two linear regions can be observed in  $\ln(f_m)$  vs.  $1/T$ , marked by the fitted red straight lines in the inset of Figure 1b. From the fits, the corresponding activation energy values were obtained, yielding  $E_{AL} = 0.29$  eV (low T) and  $E_{AL} = 0.062$  eV (high T) for relaxation A and  $E_{BL} = 0.59$  eV (low T) and  $E_{BH} = 0.64$  eV (high T) for relaxation B. These changes in the activation energies with an increasing temperature are consistent with the presence of structural changes indicative of the stabilization of a ferroelectric phase at room temperature that transforms into a paraelectric phase at high temperatures.

Figure 1d shows the temperature dependence of the real and imaginary (inset) parts of the electric permittivity of MDABCO-NH<sub>4</sub>Cl<sub>3</sub>. An overall increase in the real and imaginary permittivity can be observed, along with an increasing temperature, reflecting the increasing thermal energy available to the system. However, a frequency-independent change of behavior can be observed above ~398 K (a step-like change), consistent with the stabilization of a ferroelectric phase, and another (frequency-independent peak) can be seen at ~438 K, which might be due to a ferroelectric-paraelectric phase transition, as reported previously for a MDABCO-NH<sub>4</sub>I<sub>3</sub> analog. Both dielectric changes occur at temperatures where anomalies are observed in the DSC measurements (Figure S1).

### 3.2. Pyroelectricity

The pyroelectric coefficient was measured on a polycrystalline sample (a pellet) of MDABCO-NH<sub>4</sub>Cl<sub>3</sub> perovskite until the Curie temperature was reached, as shown in Figure 2. The maximum value achieved was around 290  $\mu\text{C K}^{-1} \text{m}^{-2}$ . The maximum occurred in the temperature region of 398–426 K at temperatures where there is a change in slope in the real and imaginary components of the electric permittivity, as shown in Figure 1d. This indicates the presence of structural changes inside the MDABCO-NH<sub>4</sub>Cl<sub>3</sub> sample that are associated with the phase transition reported for this perovskite family. The measured pyroelectric coefficient is comparable to that reported for MDABCO-NH<sub>4</sub>I<sub>3</sub> and the organic ferroelectric triglycine sulfate (TGS), which are reported to achieve maxima of 194  $\mu\text{C K}^{-1} \text{m}^{-2}$  and 306  $\mu\text{C K}^{-1} \text{m}^{-2}$ , respectively, in the polar to non-polar phase transition [31]. The second maximum occurring in the temperature interval of 431–440 K is also consistent with the second anomaly observed in the temperature dependence of the electric permittivity (Figure 1d) and in the DSC measurements (Figure S1).

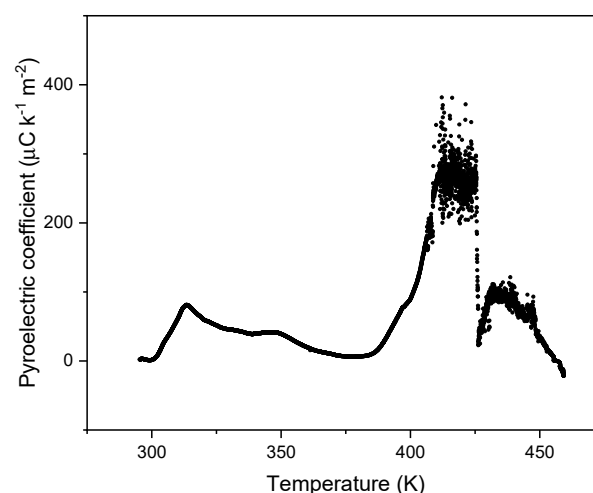


**Figure 2.** Pyroelectric coefficient as a function of the temperature of MDABCO-NH<sub>4</sub>Cl<sub>3</sub>, measured during heating.

### 3.3. Piezoelectric Characterization

The piezoelectric characteristics of electrospun nanofiber mats fabricated from MDABCO-NH<sub>4</sub>Cl<sub>3</sub>@PVC were measured at a frequency of 3 Hz under an applied force of 3 N as shown in Figure 3. The open-circuit voltage,  $V_{oc}$ , reached 12 V for the MDABCO-NH<sub>4</sub>Cl<sub>3</sub>@PVC nanofiber PENG. Note that at 3 Hz, the frequency is low enough to allow the fiber mat to return to its native microscopic structure before the next force is applied.

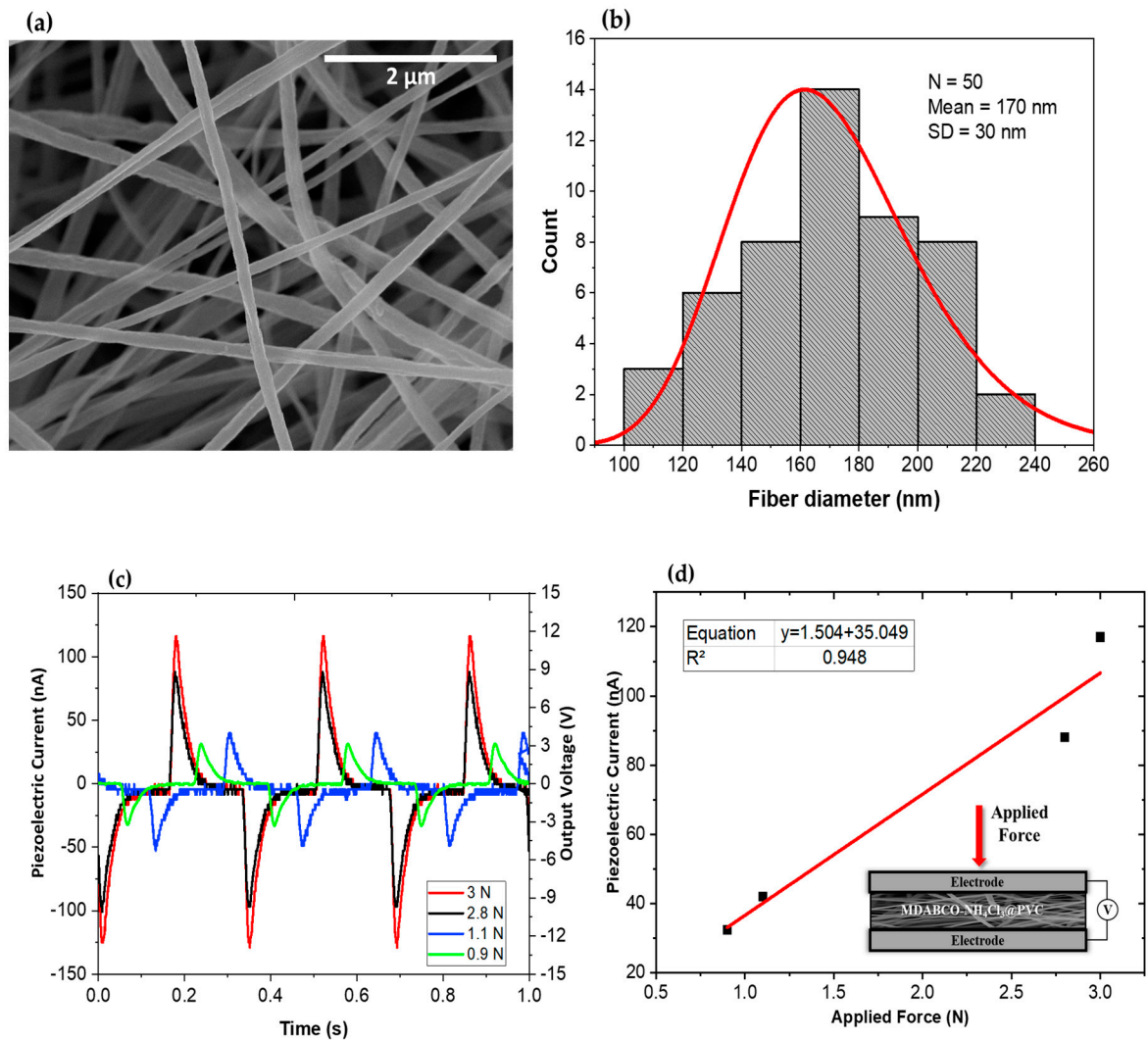


**Figure 3.** (a) SEM image at a magnification level of 50,000 $\times$  and (b) the respective fiber diameter distribution histogram for MDABCO-NH<sub>4</sub>Cl<sub>3</sub>@PVC fiber mat. The fiber diameter mean value and standard deviation were used to generate the logarithmic normal distribution represented by the curve. (c) Time dependence of the output voltage and piezoelectric current from MDABCO-NH<sub>4</sub>Cl<sub>3</sub> incorporated into PVC polymer nanofibers, and (d) plot of piezoelectric current versus applied force with a schematic piezoelectric-energy-harvesting setup with a MDABCO-NH<sub>4</sub>Cl<sub>3</sub>@PVC fiber array.

The generated piezoelectric charge, calculated from  $Q = \int Idt$  (C), amounts to 125 pC for the MDABCO-NH<sub>4</sub>Cl<sub>3</sub>@PVC mat. To reach this value, a response time of approximately 1 ms was estimated, while the maximum  $I_{sc}$  measured was 125 nA. The effective piezoelectric coefficient, calculated as  $d_{eff} = Q/F$  (pC N<sup>-1</sup>), is 42 pC N<sup>-1</sup> for MDABCO-NH<sub>4</sub>Cl<sub>3</sub>@PVC when subject to a 3N periodic force. Comparatively, the piezoelectric coefficient reported for a single MDABCO-NH<sub>4</sub>I<sub>3</sub> crystal is  $d_{33} = 14$  pC N<sup>-1</sup> along the [111] direction [27], which is three times lower. The obtained value of 42 pC N<sup>-1</sup> for MDABCO-NH<sub>4</sub>Cl<sub>3</sub>@PVC is of a similar magnitude to that displayed by the electrospun fiber mats MDABCO-NH<sub>4</sub>I<sub>3</sub>@PMMA

and MDABCO-NH<sub>4</sub>I<sub>3</sub>@PA66, reported to be 64 pC N<sup>-1</sup> and 21 pC N<sup>-1</sup>, respectively [26]. It is important to note that, for this hybrid perovskite PENG, the piezoelectric polymer (d<sub>31</sub> ~ 1.5 pC N<sup>-1</sup>) [32] contributes a small amount.

The peak power density,  $P = I_{sc}/A$  (μW m<sup>-2</sup>) (where A is the electrode area), delivered by the MDABCO-NH<sub>4</sub>Cl<sub>3</sub>@PVC mat was 310 μW m<sup>-2</sup>, around six times smaller than that delivered by the MDABCO-NH<sub>4</sub>I<sub>3</sub>@PVC fiber mat, which amounted to 1960 μW m<sup>-2</sup>.

The potential of a material as a piezoelectric sensor can be quantified by its piezoelectric voltage coefficient  $g_{eff}$ , defined as

$$g_{eff} = d_{eff}/(\epsilon' \epsilon_0) \text{ V mN}^{-1}.$$

The dielectric measurements indicate a dielectric permittivity of  $\epsilon' = 7.5$  at 20 Hz and 300 K for MDABCO-NH<sub>4</sub>Cl<sub>3</sub>@PVC nanofiber mats, which accounts for  $g_{eff} = 0.65 \text{ V mN}^{-1}$ . This high piezoelectric voltage coefficient is twice that displayed by polyvinylidene fluoride (PVDF) polymer thin films ( $g_{eff} = 0.29 \text{ V mN}^{-1}$ ) [33] and similar to that of the layered lead perovskite (4-aminotetrahydropyran)2PbBr<sub>4</sub> ( $g_{eff} = 0.67 \text{ V mN}^{-1}$ ) [7]. The obtained result is among the higher values recorded for the effective piezoelectric coefficient of electrospun fibers incorporating active organic piezoelectric materials [34–36].

#### 4. Conclusions

The synthesis and characterization of MDABCO-NH<sub>4</sub>Cl<sub>3</sub> crystals presented in this study offer valuable information on the potential applications of lead-free organic ferroelectric perovskites. This material's high-temperature paraelectric structure transitions into a ferroelectric phase at 432 K, making it suitable for room-temperature ferroelectric applications. Moreover, the pyroelectric coefficient value obtained for MDABCO-NH<sub>4</sub>Cl<sub>3</sub>, namely, 290 μC K<sup>-1</sup> m<sup>-2</sup>, is competitive with respect to values reported for MDABCO-NH<sub>4</sub>I<sub>3</sub> and the semiorganic ferroelectric triglycine sulfate (TGS), namely, 194 μC K<sup>-1</sup> m<sup>-2</sup> and 306 μC K<sup>-1</sup> m<sup>-2</sup>, respectively, at the ferroelectric-paraelectric phase transition.

The successful incorporation of MDABCO-NH<sub>4</sub>Cl<sub>3</sub> into PVC nanofibers, together with the observation of good morphological characteristics, underlines the viability of using these materials in practical devices. The observed piezoelectric properties, namely, a measured piezoelectric coefficient of 42 pC/N under a periodic force of 3 N, a peak power density of 310 μW m<sup>-2</sup>, and a piezoelectric voltage coefficient of  $g_{eff} = 0.65 \text{ V mN}^{-1}$ , all reinforce this material's potential for energy-harvesting applications.

**Supplementary Materials:** The following supporting information can be downloaded at <https://www.mdpi.com/article/10.3390/micro4020014/s1>. Figures S1 and S2: DSC and TGA spectra; Figure S3. XRD spectra; Figure S4: FTIR-ATR spectrum.

**Author Contributions:** Initial concept and planning, R.M.F.B. and E.d.M.G.; synthesis and experimental measurements, R.M.F.B., B.S., J.O., B.A., C.C., P.V.R., A.M. and M.B.; data analysis, manuscript preparation, editing and revision R.M.F.B., E.d.M.G., B.A. and M.B.; supervision, R.M.F.B. and E.d.M.G.; project administration, R.M.F.B. and E.d.M.G.; funding acquisition, R.M.F.B., B.A., M.B. and E.d.M.G. All authors have read and agreed to the published version of the manuscript.

**Funding:** This research was funded by Fundação para a Ciência e Tecnologia through FEDER (European Fund for Regional Development)-COMPETE-QREN-EU (ref. UID/FIS/04650/2013 and UID/FIS/04650/2019); E-Field—“Electric-Field Engineered Lattice Distortions (E-FiELD) for optoelectronic devices”, ref.: PTDC/NAN-MAT/0098/2020; Gemis—“Graphene-enhanced electro-magnetic interference shielding”, Ref.: POCI-01-0247-FEDER-045939 and “Non-linear phononics: Manipulating the hidden quantum phases and dynamical multiferroicity”, Ref. 2022.03564.PTDC.

**Institutional Review Board Statement:** This study did not involve humans or animals.

**Informed Consent Statement:** This study did not involve humans or animals.

**Data Availability Statement:** The raw data supporting the conclusions of this article will be made available by the authors on request.

**Acknowledgments:** We acknowledge national funds (OE) obtained through FCT—Fundação para a Ciência e a Tecnologia, I.P. in the scope of the framework contract set out in numbers 4, 5, and 6 of article 23 of the Decree-Law 57/2016 of August 29, changed by Law 57/2017 of July 19. DL 57/2016/CP1377/CT0064 (DOI: 10.54499/DL57/2016/CP1377/CT0064).

**Conflicts of Interest:** The authors declare no conflicts of interest.

## References

1. Lines, M.E.; Glass, A.M. *Principles and Applications of Ferroelectrics and Related Materials*; Oxford University Press: Oxford, UK, 2001.
2. Zhou, X.; Ke, Q.; Tang, S.; Luo, J.; Lu, Z. Ultraviolet photodetectors based on ferroelectric depolarization field. *J. Energy Chem.* **2023**, *77*, 487–498. [[CrossRef](#)]
3. Zhou, X.; Lu, Z.; Zhang, L.; Ke, Q. Wide-bandgap all-inorganic lead-free perovskites for ultraviolet photodetectors. *Nano Energy* **2023**, *117*, 108908. [[CrossRef](#)]
4. Martínez-Goyeneche, L.; Gil-Escrig, L.; Susic, I.; Tordera, D.; Bolink, H.J.; Sessolo, M. Narrowband Monolithic Perovskite-Perovskite Tandem Photodetectors. *Adv. Opt. Mater.* **2022**, *10*, 2201047. [[CrossRef](#)]
5. Cross, E. Lead-free at last. *Nature* **2004**, *432*, 24–25. [[CrossRef](#)]
6. Saito, Y.; Takao, H.; Tani, T.; Nonoyama, T.; Takatori, K.; Homma, T.; Nagaya, T.; Nakamura, M. Lead-free piezoceramics. *Nature* **2004**, *432*, 84–87. [[CrossRef](#)]
7. Chen, X.-G.; Song, X.-J.; Zhang, Z.-X.; Li, P.-F.; Ge, J.-Z.; Tang, Y.-Y.; Gao, J.-X.; Zhang, W.-Y.; Fu, D.-W.; You, Y.-M.; et al. Two-Dimensional Layered Perovskite Ferroelectric with Giant Piezoelectric Voltage Coefficient. *J. Am. Chem. Soc.* **2020**, *142*, 1077–1082. [[CrossRef](#)]
8. Guo, T.-M.; Gong, Y.-J.; Li, Z.-G.; Liu, Y.-M.; Li, W.; Li, Z.-Y.; Bu, X.-H. A New Hybrid Lead-Free Metal Halide Piezoelectric for Energy Harvesting and Human Motion Sensing. *Small* **2022**, *18*, 2103829. [[CrossRef](#)]
9. Zhang, H.-Y.; Tang, Y.-Y.; Shi, P.-P.; Xiong, R.-G. Toward the Targeted Design of Molecular Ferroelectrics: Modifying Molecular Symmetries and Homochirality. *Acc. Chem. Res.* **2019**, *52*, 1928–1938. [[CrossRef](#)]
10. Li, W.; Wang, Z.; Deschler, F.; Gao, S.; Friend, R.H.; Cheetham, A.K. Chemically diverse and multifunctional hybrid organic-inorganic perovskites. *Nat. Rev. Mater.* **2017**, *2*, 16099. [[CrossRef](#)]
11. Valasek, J. Properties of Rochelle Salt Related to the Piezo-electric Effect. *Phys. Rev.* **1922**, *20*, 639–664. [[CrossRef](#)]
12. Valasek, J. Piezo-Electric and Allied Phenomena in Rochelle Salt. *Phys. Rev.* **1921**, *17*, 475–481. [[CrossRef](#)]
13. Song, X.; Hodes, G.; Zhao, K.; Liu, S. Metal-Free Organic Halide Perovskite: A New Class for Next Optoelectronic Generation Devices. *Adv. Energy Mater.* **2021**, *11*, 2003331. [[CrossRef](#)]
14. Chu, L.-L.; Zhang, T.; Zhang, W.-Y.; Shi, P.-P.; Gao, J.-X.; Ye, Q.; Fu, D.-W. Three-Dimensional Metal-Free Molecular Perovskite with a Thermally Induced Switchable Dielectric Response. *J. Phys. Chem. Lett.* **2020**, *11*, 1668–1674. [[CrossRef](#)]
15. You, Y.-M.; Liao, W.-Q.; Zhao, D.; Ye, H.-Y.; Zhang, Y.; Zhou, Q.; Niu, X.; Wang, J.; Li, P.-F.; Fu, D.-W.; et al. An organic-inorganic perovskite ferroelectric with large piezoelectric response. *Science* **2017**, *357*, 306–309. [[CrossRef](#)]
16. Saparov, B.; Mitzi, D.B. Organic-Inorganic Perovskites: Structural Versatility for Functional Materials Design. *Chem. Rev.* **2016**, *116*, 4558–4596. [[CrossRef](#)]
17. Kamat, P.V.; Bisquert, J.; Buriak, J. Lead-Free Perovskite Solar Cells. *ACS Energy Lett.* **2017**, *2*, 904–905. [[CrossRef](#)]
18. Boix, P.P.; Agarwala, S.; Koh, T.M.; Mathews, N.; Mhaisalkar, S.G. Perovskite Solar Cells: Beyond Methylammonium Lead Iodide. *J. Phys. Chem. Lett.* **2015**, *6*, 898–907. [[CrossRef](#)]
19. Doshi, J.; Reneker, D.H. Electrospinning process and applications of electrospun fibers. *J. Electrostat.* **1995**, *35*, 151–160. [[CrossRef](#)]
20. Reneker, D.H.; Chun, I. Nanometre diameter fibres of polymer, produced by electrospinning. *Nanotechnology* **1996**, *7*, 216–223. [[CrossRef](#)]
21. Ramakrishna, S.; Fujihara, K.; Teo, W.-E.; Yong, T.; Ma, Z.; Ramaseshan, R. Electrospun nanofibers: Solving global issues. *Mater. Today* **2006**, *9*, 40–50. [[CrossRef](#)]
22. Isakov, D.V.; de Matos Gomes, E.; Vieira, L.G.; Dekola, T.; Belsley, M.S.; Almeida, B.G. Oriented single-crystal-like molecular arrangement of optically nonlinear 2-methyl-4-nitroaniline in electrospun nanofibers. *ACS Nano* **2011**, *5*, 73–78. [[CrossRef](#)]
23. Richard-Lacroix, M.; Pellerin, C. Molecular Orientation in Electrospun Fibers: From Mats to Single Fibers. *Macromolecules* **2013**, *46*, 9473–9493. [[CrossRef](#)]
24. Rørvik, P.M.; Grande, T.; Einarsrud, M.-A. One-Dimensional Nanostructures of Ferroelectric Perovskites. *Adv. Mater.* **2011**, *23*, 4007–4034. [[CrossRef](#)]
25. Isakov, D.; de Matos Gomes, E.; Almeida, B.; Kholkin, A.L.; Zelenovskiy, P.; Neradovskiy, M.; Shur, V.Y. Energy harvesting from nanofibers of hybrid organic ferroelectric dabcO<sub>4</sub>HReO<sub>4</sub>. *Appl. Phys. Lett.* **2014**, *104*, 032907. [[CrossRef](#)]
26. Baptista, R.M.F.; Moreira, G.; Silva, B.; Oliveira, J.; Almeida, B.; Castro, C.; Rodrigues, P.V.; Machado, A.; Belsley, M.; de Matos Gomes, E. Lead-Free MDABCO-NH<sub>4</sub>I<sub>3</sub> Perovskite Crystals Embedded in Electrospun Nanofibers. *Materials* **2022**, *15*, 8397. [[CrossRef](#)]
27. Ye, H.-Y.; Tang, Y.-Y.; Li, P.-F.; Liao, W.-Q.; Gao, J.-X.; Hua, X.-N.; Cai, H.; Shi, P.-P.; You, Y.-M.; Xiong, R.-G. Metal-free three-dimensional perovskite ferroelectrics. *Science* **2018**, *361*, 151–155. [[CrossRef](#)]

28. Wang, H.; Liu, H.; Zhang, Z.; Liu, Z.; Lv, Z.; Li, T.; Ju, W.; Li, H.; Cai, X.; Han, H. Large piezoelectric response in a family of metal-free perovskite ferroelectric compounds from first-principles calculations. *NPJ Comput. Mater.* **2019**, *5*, 17. [[CrossRef](#)]
29. Marino, M.G.; Kreuer, K.D. Alkaline Stability of Quaternary Ammonium Cations for Alkaline Fuel Cell Membranes and Ionic Liquids. *Chemsuschem* **2015**, *8*, 513–523. [[CrossRef](#)]
30. Kremer, F.; Schönhals, A. *Broadband Dielectric Spectroscopy*; Springer Science & Business Media: Berlin/Heidelberg, Germany, 2003.
31. Ghane-Motlagh, R.; Kroener, M.; Goldschmidtboeing, F.; Danilewsky, A.N.; Woias, P. A dynamic method for the measurement of pyroelectric properties of materials. *Smart Mater. Struct.* **2018**, *27*, 084004. [[CrossRef](#)]
32. Bharti, V.; Kaura, T.; Nath, R. Improved piezoelectricity in solvent-cast PVC films. *IEEE Trans. Dielectr. Electr. Insul.* **1995**, *2*, 1106–1110. [[CrossRef](#)]
33. Li, M.Y.; Wondergem, H.J.; Spijkman, M.J.; Asadi, K.; Katsouras, I.; Blom, P.W.M.; de Leeuw, D.M. Revisiting the delta-phase of poly(vinylidene fluoride) for solution-processed ferroelectric thin films. *Nat. Mater.* **2013**, *12*, 433–438. [[CrossRef](#)]
34. Baptista, R.M.F.; Lopes, P.E.; Rodrigues, A.R.O.; Cerca, N.; Belsley, M.S.; de Matos Gomes, E. Self-assembly of Boc-p-nitro-l-phenylalanyl-p-nitro-l-phenylalanine and Boc-l-phenylalanyl-l-tyrosine in solution and into piezoelectric electrospun fibers. *Mater. Adv.* **2022**, *3*, 2934–2944. [[CrossRef](#)]
35. Baptista, R.M.F.; de Matos Gomes, E.; Raposo, M.M.M.; Costa, S.P.G.; Lopes, P.E.; Almeida, B.; Belsley, M.S. Self-assembly of dipeptide Boc-diphenylalanine nanotubes inside electrospun polymeric fibers with strong piezoelectric response. *Nanoscale Adv.* **2019**, *1*, 4339–4346. [[CrossRef](#)]
36. Bernardo, C.R.; Baptista, R.M.F.; de Matos Gomes, E.; Lopes, P.E.; Raposo, M.M.M.; Costa, S.P.G.; Belsley, M.S. Anisotropic PCL nanofibers embedded with nonlinear nanocrystals as strong generators of polarized second harmonic light and piezoelectric currents. *Nanoscale Adv.* **2020**, *2*, 1206–1213. [[CrossRef](#)]

**Disclaimer/Publisher’s Note:** The statements, opinions and data contained in all publications are solely those of the individual author(s) and contributor(s) and not of MDPI and/or the editor(s). MDPI and/or the editor(s) disclaim responsibility for any injury to people or property resulting from any ideas, methods, instructions or products referred to in the content.